Analysis and Correction of Smeared Image From Interline-Transfer CCD in Beam Quality Measurement

Jie Luo, Laian Qin ⬨, Zaihong Hou, Wenyue Zhu, Feng He, Wenlu Guan, and Yilun Cheng

Abstract—**The smear effect caused by light penetration of interline-transfer (IT) CCD in beam quality measurement (BQM) is detrimental and not analyzed pertinently. This report proposes a mathematical model and a correction method for the smeared image. The smear noise is fitted and subtracted through its correlation with the light signal obtained from the model and pre-calibration. The application in BQM is presented by measuring beam quality factor M^2 and power in the bucket (PIB). The results verify the validity of the method. An evaluation standard of the correction effect is also recommended.**

Index Terms—**Charge-coupled-device (CCD) image sensor, interline transfer (IT), laser beams.**

I. INTRODUCTION

CCD sensors are widely used in beam quality measurement (BQM) to image the cross-section spot and reproduce its intensity distribution [1], [2], [3], [4]. Interline-transfer (IT) CCD is one of the most typical structures. Its signal charges are transferred from the photodiode to the vertical CCD (V-CCD) after the photosensitivity, then enter the horizontal CCD (H-CCD) for amplification and readout [5]. IT-CCD has a balanced performance in terms of high frame rate, imaging quality and sensitivity [6], [7], [8]. The smear effect is a common error source for IT-CCD, which is caused by light penetration through the light shield on VCCD, light leakage from diffraction, refraction, and waveguide effect on CCD surface, or charge diffusion during signal transfer in V-CCD [9], [10]. Generally, it appears as vertical line noise across the image.

Some semiconductor processes and pixel structure designs that suppress the smear effect provide significant references for sensor development. Optimizations for P-N junctions can effectively reduce charge diffusion in the p-well below the photodiode [11], [12], [13], [14]. Moreover, double layer design and material replacement of the light shield can further avoid light penetration [7], [8], [15], [16]. Furthermore, the optimization of on-chip lenses used to guide light onto photodiodes was reported, which controls light leakage [17]. Some electrical methods are also effective, such as a special clocking mode to dump noise charge before the image readout [6], [18].

Correction algorithms are an attractive alternative to hardware design and electrical processing due to their convenience and applicability for the generated smeared image [19], [20]. Using the optical black area (OBR) [19] and dummy pixel [20] is a comprehensible research direction without the analysis of the causes of the smear effect. The noise can be estimated from the area without a valid light signal, and the smeared image can be effectively corrected through appropriate filters. Nevertheless, the premise is that the image has an area that is unexposed and easy to extract. Establishing a theoretical model to solve the noise mathematically is a potential idea. Several reliable results have been published about frame transfer CCD (FT-CCD) [21], [22], [23]. In contrast, because the smear effect of IT-CCD has more complex contributing factors [9], it is challenging to do a universal mathematics analysis.

However, in BQM, the factors of the smear effect are limited and analyzable, which provides feasibility to analyze mathematically. The smear effect is usually caused by low quantum efficiency (QE) and short exposure time. This situation is common in BQM. For instance, the Silicon camera is a frequent substitute for the InGaAs camera in measuring near-infrared laser beams. Although the latter has a higher QE, its cost is much higher, and the thermal noise is noticeable [24]. Also, the short exposure time has advantages in taking the details on the time axis and preventing the response threshold from being exceeded. In this case, the light intensity to reach the CCD sensor is relatively strong for sufficient response value and dynamic response range. This intensity is not too high to damage the sensor, so the measurement is safe. However, it will result in strong light penetration in the aluminum mask on the V-CCD. When signal charges are transferred to H-CCD line by line under the effect of the readout pulse from V-CCD, noise charges caused by light penetration are mixed in. In principle, the noise on any

pixel finally read out will be related to the total amount of light penetration in this column and the pixel transfer time in V-CCD. Finally, there is a strong smear effect on the image because the light penetration on the pixel scale accumulated in the whole column [17], [18]. In summary, light penetration is considered the main factor of the smear effect. Based on this, the correlation between noise and signal is expected to be solved according to the mathematical analysis. The expression is related to the working wavelength, exposure time and pixel transfer time. The first two are generally known, while the last one is fixed to the camera, which generally at microsecond level. It is believed that the expression parameters can be obtained from the camera pre-calibration. Finally, the noise can be corrected through the expression in subsequent series measurements.

Following the above contents, this report introduces the image feature and proposes a mathematical model of the smear effect for IT-CCD in BQM (Section II), shows the experiment results of pre-calibration and correction by the model to various spots (Section III), achieves BQM by the correction, and provides relevant evaluation criteria (Section IV). This work provides the following main contributions.

1) A reliable mathematical model of the smear effect for IT-CCD in BQM.
2) A complete, effective method and the related validation for correcting smeared images in BQM.
3) A reference for the studies related to the smear effect caused by light penetration in other fields, such as the millimeter wave lidar or fast imaging in strong light.

II. SMEAR MODEL FOR IT-CCD

Analyzing the actual image feature is necessary to establish a reliable model, so a typical imaging in BQM is set. A silicon IT-CCD camera takes the cross-sectional spots at 1064 nm, and the total power is around 10 mW. The QE is less than 2%, and the exposure time is between 10 and 100 μs.

A. Image Feature

Fig. 1(a), (b) and (c) show the same cross-section spot with a diameter of around 9mm, which are taken by IT-CCD and CMOS camera, respectively. The comparison emphasizes the line smear noise. It is worth noting that the CMOS camera is selected as the control group because it has no structure to produce the smear effect. However, considering image quality and other noise, it is not a perfect alternative to the CCD camera in this application.

The line noise will have a negative impact on the measurement of the centroid position and beam width of the spot, resulting in a significant error in BQM. According to Fig. 1(c), the lateral width of the line noise is larger than the diameter of the spot, which means that not all the noises are caused by the incident light in the same column. Fig. 1(d), (e) and (f) are the spots with a diameter of around 2 mm. It can be noticed that the line noise is divided into several thinner lines. To distinguish, the brightest one in the middle is called the main line, and the lines on both sides, which seem to be symmetrically distributed with the main line as the axis, are called the sub-lines. The same rule also exists in the 9 mm spot. The main line and the sub-lines overlap
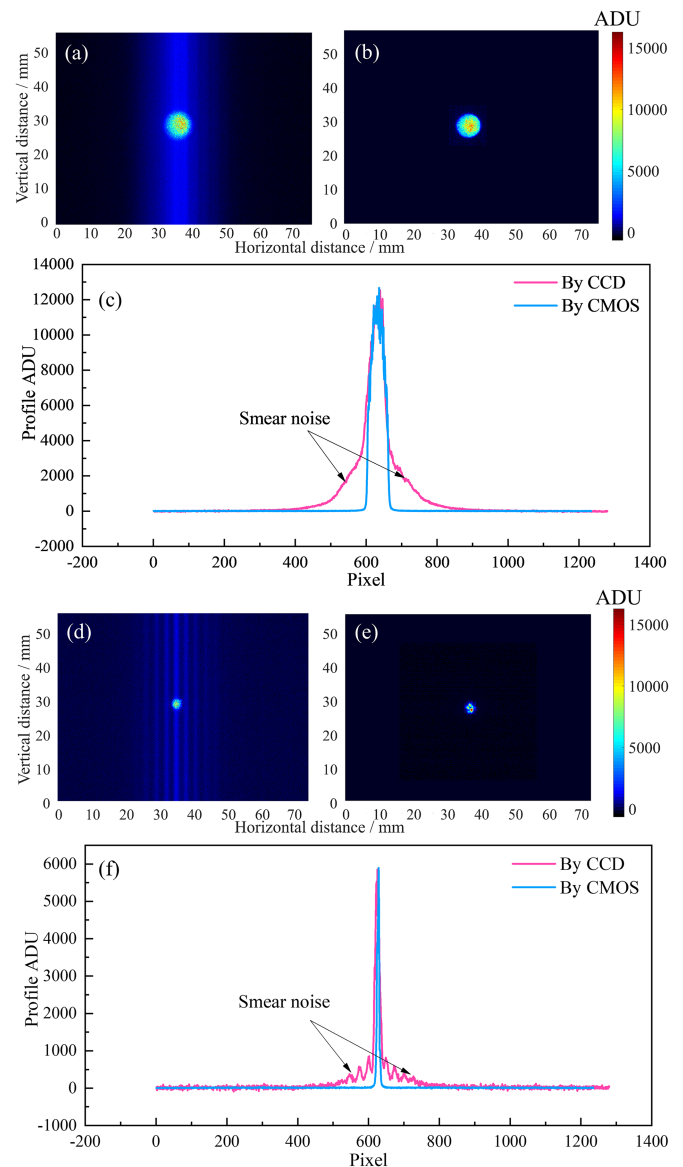

Fig. 1. (a)The smeared image of a spot with a diameter of around 9 mm taken by an IT-CCD camera and the exposure time is 20 μs, and light source is around 10 mW, and ADU means Analog-to-Digital Unit; (b) The image of the spot of Fig. 1 (a) taken by a CMOS camera at 50 μs and 10 mW; (c) The centr-oid profiles of Fig. 1 (a) and (b); (d)The smeared image of a spot with a diam-eter of around 2 mm taken by an IT-CCD camera at 50 μs and 4 mW; (e) The image of the spot of Fig. 1 (d) taken by a CMOS camera at 100 μs and 4 mW; (f) The centroid profiles of Fig. 1 (d) and (e).

and are visually indistinguishable since their width increase as the spot diameter increases. As for the reason for the sub-lines, the diffraction is excluded because no bright diffraction spot is observed in the sub-lines. Moreover, there is no diffraction or other optical phenomenon in the image from the CMOS camera for the same light source. This kind of noise should be analyzed as a nonrandom pattern noise. The validity of this analysis will also be verified in the pre-calibration.

Another method of extracting noise is needed to discuss the numerical feature of the smeared image. The CMOS image is unavailable because of the difference in resolution, photoelectric conversion efficiency and exposure time with the CCD. The
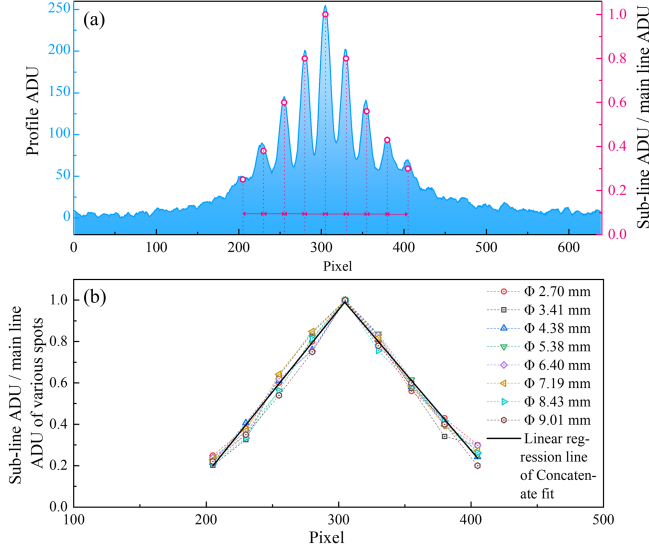
Fig. 2. (a) The profile of line noise from the image for a 2 mm spot. (b) the multiple relationships between the sub-lines and the main line of various spots, which conforms to linear regression. The total goodness of concatenated fitting is 0.986.

method is supposed to be reliable but does not need to consider convenience and applicability because of the controllable experimental environment. Therefore, OBR [19] is selected to extract the line noise in images of spots with different sizes, powers and shapes. As shown in Fig. 2(a), a profile of the smear noise consisting of a main line and the multilevel sub-lines exemplifies the extraction result. Fig. 2(b) shows the multiple relationships between the sub-lines and the main line of various spots. This result is calculated by deconvolution because the image is the superposition of multiple lines. According to Fig. 2, the smeared image for IT-CCD shows the following numerical characteristics:

1) The multiple relationships between the sub-lines and the main line conform to linear regression.
2) The distances between adjacent lines are equal and fixed.
3) The slope and intercept of the linear correlation do not change significantly with the spot's size, power, and shape. The total goodness of concatenated fitting of various spots is 0.986. The fitting goodness R^2 is calculated as

$$R^2 = \frac{SSR}{SST} = \frac{\sum_{i=1}^{n}(f_i - \bar{y})^2}{\sum_{i=1}^{n}(y_i - \bar{y})^2}, \qquad (1)$$

where SSR is the sum of squares for regression and SST is the sum of squares for total. Also, y represents source data and f represents fit data.

According to the image feature of the smear effect caused by light penetration, it is believed that the main line is caused by the light signal in the same column, while the sub-lines follow the main line. Next, finding the relationship between the line noise and the light signal represented by the spot's intensity distribution is necessary. Then the smeared image can be corrected because it is the sum of light signal and noise.

B. Mathematical Theory

Based on Section II.A, the Total Smear Noise N Can Be Expressed As

$$N = N_0 + N_{l1} + N_{r1} + N_{l2} + N_{r2} + \cdots, \qquad (2)$$

where N_0 is the main line, N_{lx} and N_{rx} represent the sub-line of level x on the left and right. The closer to the main line, the smaller x is. As shown in Fig. 2, about the fifth and the following sub-lines can be ignored because they are submerged in dark current noise. The original smeared image $O(i, j)$ taken by the IT-CCD camera can be represented by

$$O(i,j) = t_0 I(i,j) + N(i,j), i \in [1,m], j \in [1,n], \qquad (3)$$

where i and j respectively represent the row and the column number where the pixel is located, and there are all m rows and n columns of pixels in the image. $N(i, j)$ and $I(i, j)$ represent the noise and the relative light intensity, respectively, and t_0 represents exposure time. In application, $O(i, j)$ and t_0 are known, but $I(i, j)$, representing the corrected image, is supposed to be solved.

First, the relationship between $N(i, j)$ and $I(i, j)$ needs a solution. By the signal transfer principle, $N_0(i, j)$ is caused by the total light intensity of the column and is linearly related to $\sum_{i=1}^{m} I(i, j)$, as shown in (3). The line noise of each row is equal, so N_0 and the other line noise will only be related to the column number j as

$$N_0(j) = k_0 \sum_{i=1}^{m} I(i,j). \qquad (4)$$

(3) is substituted into (1), then there is

$$N(j) = k_0 \sum_{i=1}^{m} I(i,j) + k_{l1} \sum_{i=1}^{m} I(i,j+d) + k_{r1} \sum_{i=1}^{m} I(i,j-d)$$
$$+ k_{l2} \sum_{i=1}^{m} I(i,j+2d) + k_{r2} \sum_{i=1}^{m} I(i,j-2d) + \cdots, \qquad (5)$$

where k_x represents the multiple of $N_x(i, j)$ to $\sum_{i=1}^{m} I(i, j)$, and d is the distance between adjacent lines. For ease of calculation, the functions $f_N(j)$ and $f_I(j)$ are used to fit the discrete $N(j)$ and $\sum_{i=1}^{m} I(i, j)$. It is worth noting that the defined domains of the two functions are different, so their intersection $j \in [jl, jr]$ is taken. jl and jr are the left and right column numbers where $\sum_{i=1}^{m} I(i, j)$ reduces to near zero. So there is

$$f_N(j) = k_0 f_I(j) + k_{l1} f_I(j+d) + k_{r1} f_I(j-d)$$
$$+ k_{l2} f_I(j+2d) + k_{r2} f_I(j-2d) + \cdots, j \in [jl, jr]. \qquad (6)$$

Then solve the derivative of $f_N(j)$ with respect to $f_I(j)$ as

$$f_N'(f_I) = \frac{df_N}{df_I} = \frac{df_N}{dj}\frac{dj}{df_I} = \frac{f_N'(j)}{f_I'(j)}$$
$$= k_0 + k_{l1} + k_{r1} + k_{l2} + k_{r2} + \cdots, j \in [jl, jr]. \qquad (7)$$
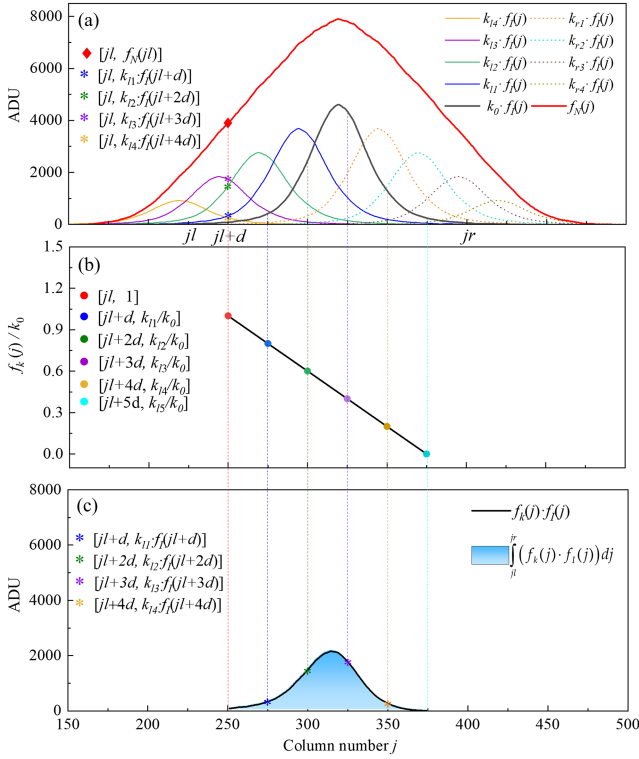
Fig. 3. (a) $f_k(j) \cdot f_I(j)$ of the main line and different sub-lines and total noise $f_N(j)$ expressed by ADU. The asterisks with different colors represent the contributions of different sub-lines to the total noise at $j = jl$. (b) $f_k(j)/k_0$. The dots with different colors represent multiple relations belonging to different sub-lines. (c) $f_k(j) \cdot f_I(j)$ of the main line and its integral. The asterisks with different colors represent the correspondences of the sub-lines contribution to the main line.

(6) proves that $N(j)$ and $\sum_{i=1}^{m} I(i,j)$ conform to linear regression with a slope of $k_0 + k_{l1} + k_{r1} + k_{l2} + k_{r2} + \cdots$. To determine the complete expression, solving the intercept is necessary. It can be found that when $\sum_{i=1}^{m} I(i,j)$ is near zero, $N(j)$ can be regarded as the Y-axis intercept. At this time, j is equal to jl or jr. Take jl as an example, so there is

$$\sum_{i=1}^{m} I(i, jl) = \sum_{i=1}^{m} I(i, jl - d) = \sum_{i=1}^{m} I(i, jl - 2d) = \cdots = 0.$$

$$(8)$$

The Y-axis intercept $N(jl)$ or $f_N(jl)$ is related to several sub-lines on the left, which is also related to the main line, as shown in Fig. 3, which can be expressed as

$$N(jl) = k_{l1} \sum_{i=1}^{m} I(i, jl + d) + k_{l2} \sum_{i=1}^{m} I(i, jl + 2d) + \cdots,$$

$$(9)$$

and

$$f_N(jl) = k_{l1} f_I(jl + d) + k_{l2} f_I(jl + 2d) + \cdots.$$

$$(10)$$

To facilitate function operation, $f_k(j)$ is set to fit k_0, k_{l1}, k_{l2}, …, as shown in Fig. 3(b), and follows

$$f_k(j) = \begin{cases} k_0, j = jl \\ k_{l1}, j = jl + d \\ k_{l2}, j = jl + 2d \\ \vdots \end{cases} , j \in [jl, jr].$$

$$(11)$$

Then, $f_N(jl)$ is represented by the accumulation of data points multiplied by $f_k(j)$ and $f_I(j)$, which is proportional to $\int_{jl}^{jr} (f_k(j) \cdot f_I(j)) dj$, and can be further used for partial integration as

$$f_N(jl)$$
$$= f_k(jl + d) \cdot f_I(jl + d) + f_k(jl + 2d) \cdot f_I(jl + 2d) + \cdots$$
$$\propto \int_{jl}^{jr} (f_k(j) \cdot f_I(j)) \, dj$$
$$= \int_{jl}^{jr} \left(f_k(j) \cdot \left(\int f_I(j) dj \right)' \right) dj$$
$$= \left(f_k(j) \cdot \int f_I(j) dj - \int \left(f'_k(j) \cdot \int f_I(j) dj \right) dj \right) \Big|_{jl}^{jr}$$
$$= (f_k(jr) - f_k(jl)) \cdot \int_{jl}^{jr} f_I(j) dj$$
$$= (f_k(jr) - k_0) \cdot \int_{jl}^{jr} f_I(j) dj$$
$$\propto \int_{jl}^{jr} f_I(j) dj.$$

$$(12)$$

From the above, $f_N(jl)$ is proportional to $\int_{jl}^{jr} f_I(j) dj$, then it can be assumed as

$$f_N(j) = \eta_1 f_I(j) + \eta_2 \int_{jl}^{jr} f_I(j) dj, j \in [jl, jr].$$

$$(13)$$

By the analogy, there is

$$N(j) = \eta_1 \sum_{i=1}^{m} I(i,j) + \eta_2 \sum_{i=1}^{m} \sum_{j=1}^{n} I(i,j), j \in [jl, jr].$$

$$(14)$$

(13) is the relationship between $N(j)$ and $I(i,j)$. According to (6), η_1 is equal to $k_0 + k_{l1} + k_{r1} + k_{l2} + k_{r2} + \cdots$, η_2 is unknown due to the derivation of multiple proportional relations. However, both can be obtained by pre-calibrating the camera at the working wavelength.

Second, in the application, it is necessary to fit $N(j)$ from the original image $O(i,j)$ and then subtract it from $O(i,j)$ to obtain $I(i,j)$ representing the optical signal, which is calculated as follows. Accumulate (13) in the column direction as

$$\sum_{j=1}^{n} N(j) = (\eta_1 + n\eta_2) \sum_{i=1}^{m} \sum_{j=1}^{n} I(i,j), j \in [jl, jr].$$

$$(15)$$

Substitute (14) into (13), then there is

$$\sum_{i=1}^{m} I(i,j) = \frac{1}{\eta_1} N(j) - \frac{\eta_2}{\eta_1(\eta_1 + n\eta_2)} \sum_{j=1}^{n} N(j), j \in [jl, jr].$$
(16)

According to (2), accumulate (13) in the row direction as

$$\sum_{i=1}^{m} O(i,j) = t_0 \sum_{i=1}^{m} I(i,j) + mN(j).$$
(17)

Substitute (15) into (16), then there is

$$\sum_{i=1}^{m} O(i,j) = \left(\frac{t_0}{\eta_1} + m\right) N(j) - \frac{t_0 \eta_2}{\eta_1(\eta_1 + n\eta_2)} \sum_{j=1}^{n} N(j),$$

$$j \in [jl, jr].$$
(18)

To further accumulate (17) in the column direction, there is

$$\sum_{i=1}^{m}\sum_{j=1}^{n} O(i,j) = \left(\frac{t_0\eta_1 + m\eta_1^2 + mn\eta_1\eta_2}{\eta_1(\eta_1 + n\eta_2)}\right) \sum_{j=1}^{n} N(j),$$

$$j \in [jl, jr].$$
(19)

Substitute (18) into (17), then there is

$$N(j) = \frac{\eta_1}{t_0 + m\eta_1} \sum_{i=1}^{m} O(i,j)$$

$$+ \frac{t_0}{(t_0 + m\eta_1)(t_0 + m\eta_1 + mn\eta_2)} \sum_{i=1}^{m}\sum_{j=1}^{n} O(i,j),$$

$$= \left(\frac{t_0\eta_1 + m\eta_1^2 + mn\eta_1\eta_2}{\eta_1(\eta_1 + n\eta_2)}\right) \sum_{j=1}^{n} N(j),$$

$$j \in [jl, jr].$$
(20)

Substitute (19) into (2), then there is

$$I(i,j) = \frac{1}{t_0}(O(i,j) - N(j)) = \eta_a O(i,j)$$

$$+ \eta_b \sum_{i=1}^{m} O(i,j) + \eta_c \sum_{i=1}^{m}\sum_{j=1}^{n} O(i,j), j \in [jl, jr],$$
(21)

where:

$$\eta_a = \frac{1}{t_0}, \eta_b = -\frac{\eta_1}{t_0(t_0 + m\eta_1)},$$

$$\eta_c = -\frac{1}{(t_0 + m\eta_1)(t_0 + m\eta_1 + mn\eta_2)}.$$
(22)

(19) is the correlation expression between $I(i,j)$ and $O(i,j)$. It is worth noting that the expression of $N(j)$ is incomplete because the calculation where $j \in [1, jl] \cup (jr, n]$ is unavailable. The noise in this defined domain represents exactly the sub-lines in the area of no light incidence mentioned in Section II.A. However, since the optical signal is only generated in $[jl, jr]$, the expression of $I(i,j)$ is complete and does not result in missing signal resolution.
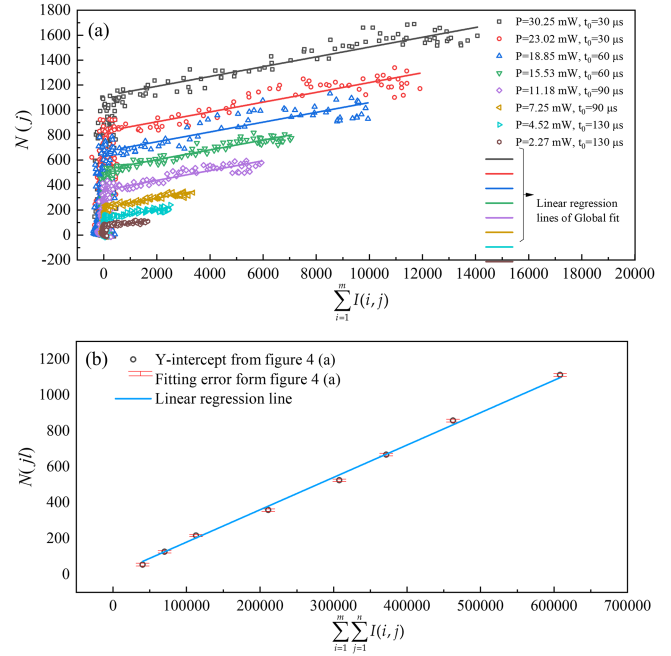

Fig. 4. (a) $N(j)$ varying with $\sum_{i=1}^{m} I(i,j)$ of different spots. P means the total power of the spot. (b) Y-axis intercept $N(jl)$ varying with $\sum_{i=1}^{m}\sum_{j=1}^{n} I(i,j)$ and the linear regression line.

This section determines the correlation between $N(j)$ and $I(i,j)$ firstly, then deduces the correlation between $I(i,j)$ and $O(i,j)$. The parameters of the expression can be obtained by pre-calibration.

III. FITTING AND CORRECTION OF SMEARED IMAGE

A. Pre-Calibration

Section II derives the correlation expression of the corrected image $I(i,j)$ and the original smeared image $O(i,j)$. The relevant parameters need to be measured by pre-calibration to the camera. The OBR method is still used because the pre-calibration experiment is also controllable. For truncated Gaussian spots with different power and size but the same wavelength of 1064 nm, use a silicon-based IT-CCD camera to take images with different exposure times t_0. Subtract $O(i,j)$ from $N(j)$ of m rows extracted from ORB to obtain $I(i,j)$, and the data from sequence images are shown in Fig. 4.

Fig. 4(a) shows the relationship between $N(j)$ and $\sum_{i=1}^{m} I(i,j)$. It can be seen that $N(j)$ rises to an obvious value when $\sum_{i=1}^{m} I(i,j)$ close to zero, especially for the spot with high total power. Notably, the slopes of different spots are similar, which is consistent with the derivation in Section II.B. Based on (13), The global linear regression fitting with uniform slope η_1 is performed in Fig. 4(a). The intercept $N(jl)$ of different spots is obtained, too. At this time, the total fitting goodness is 0.989. Then the relationship between $N(jl)$ and $\sum_{i=1}^{m}\sum_{j=1}^{n} I(i,j)$ is fitted by linear regression to solve η_2, and the fitting goodness is 0.997. Consequently, the specific relationship is available, and the sufficient fitting goodness of pre-calibration proves the derivation in Section II.
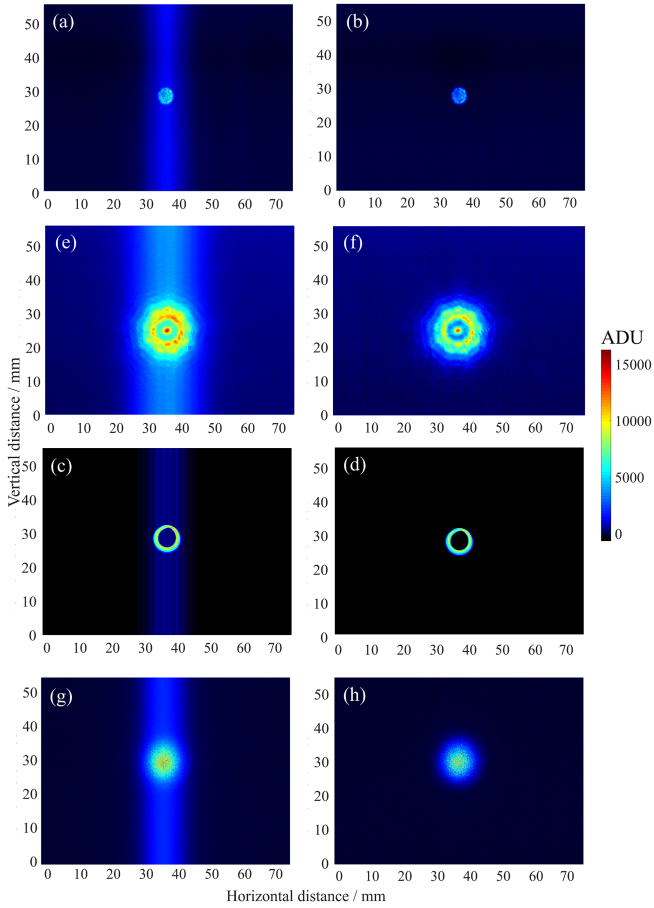
Fig. 5. (a) Broken spot in the smeared image at 120 μm and 5 mW. (b) Broken spot in the corrected image. (c) Annular spot in the smeared image at 50 μm and 20 mW. (d) Annular spot in the corrected image. (e) Diffracted spot in the smeared image at 200 μm and 4 mW. (f) Diffracted spot in the corrected image. (g) Non-truncated spot in the smeared image at 50 μm and 12 mW. (h) Non-truncated spot in the corrected image.

B. Correction Effect

Equation (20) is used to process the original smeared image in the application. The expression is simple, so the program runs fast and meets the requirement of real-time processing. Fig. 5 shows the smeared images of the cross-section spots of various beams taken by the camera pre-calibrated in Section III.A and the corrected images by fitting the line noise based on the specific expression. Considering that the truncated Gaussian spot is selected for pre-calibration, several other valuable spots in the laser field are chosen for real-time processing to verify the applicability of the correction method. There is a broken spot commonly seen in atmospheric turbulence measurement, an annular spot used for laser cutting and other fields, a diffracted spot usually seen at the outlet of the laser source, and a non-truncated spot corresponding to the one used to pre-calibrate. Their differences are not only reflected in the shape, power and exposure time but also in the imaging method. The near-infrared lens takes the spots imaged on the transmissive Lambertian in Fig. 5(a) and (c). The CCD sensor array is directly used to truncate and receive the attenuated beam in the propagation in

Fig. 5(e). The spot imaged on the reflective Lambertian are taken by the camera with lens in Fig. 5(g). These three types of imaging modes can cover the most application of BQM. The correction makes the line noise no longer visible in Fig. 5(b), (d), (f) and (g). However, to verify the feasibility of BQM using this correction, the calculation of specific beam quality evaluation parameter is still required, which will be described in detail in Section IV.
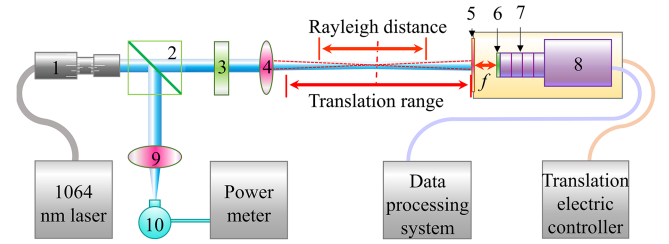

Fig. 6. BQM platform. 1-collimator, 2-spectroscope, 3-attenuator, 4-aberrationless convex lens, 5-transmitted Lambertian, 6-filter, 7-short focal lens, 8-camera, 9-lens, 10-intergrating sphere.

IV. APPLICATION IN BQM

For BQM, the correction of the smear effect should not affect the accurate calculation of quality evaluation parameter. As shown in Fig. 6, a typical BQM platform based on a CCD camera is built to test a multimode laser source at 1064 nm. A group of spots of different cross sections in the optical axis direction are obtained through camera translation shooting, and corrected in real time. Then the quality evaluation parameter is calculated according to the spot sequence. The CCD used in the experiment belongs to Sony ICX445ALA, and the camera has been pre-calibrated by a 1064 nm laser. It has a 960×1280-pixel, monochrome, and silicon-based IT-CCD with a pixel size of 10 μm combined with a near-infrared lens. The exposure time of this test is 50 μs. The image bit depth is 14-bit, and the running time of the smear correction program does not exceed 100 μs. It shall not exceed 4% of the total calculation time of BQM. The same series CMOS camera is used for the comparison experiment. Although the pixel size differs from the CCD camera's, the effect on the contrast between the evaluation parameter can be ignored.

The typical beam quality factor M^2 is selected as the evaluation parameter to the image sequence, which can comprehensively evaluate the near-field and far-field characteristics of the beam. Its conceptual calculation formula is

$$M^2 = \frac{\pi^2}{16\lambda^2} \begin{bmatrix} d_{0x}^4 \cdot \Theta_x^2 & d_{0xy}^4 \cdot \Theta_{xy}^2 \\ d_{0xy}^4 \cdot \Theta_{xy}^2 & d_{0y}^4 \cdot \Theta_y^2 \end{bmatrix}. \tag{23}$$

where x and y direction belong to the laboratory coordinate system perpendicular to z direction, which is the optical axis. d_{0x}^2 and d_{0y}^2 are the square of the beam waist width in x and y direction, respectively, and d_{0xy}^2 is the cross term of these two. Θ_x^2 and Θ_y^2 is the square of the beam divergence angle in x and y direction, respectively, and Θ_{xy}^2 is the cross term of these two. The beam waist width is calculated by the centroid coordinate
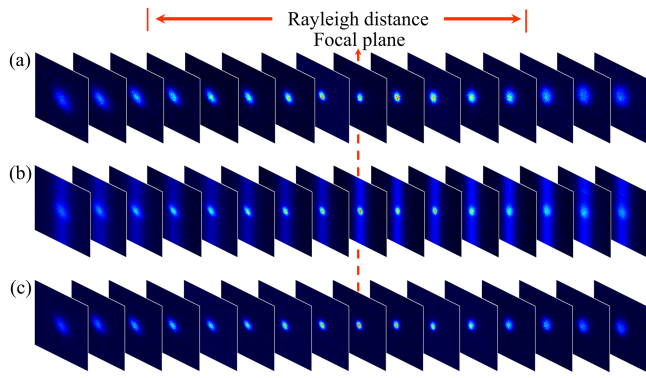
Fig. 7.   (a) The image sequence taken by CMOS camera at 100 μm and 10 mW. (a) The smeared image sequence taken by IT-CCD camera at 50 μm and 10 mW. (b) The corrected image sequence.
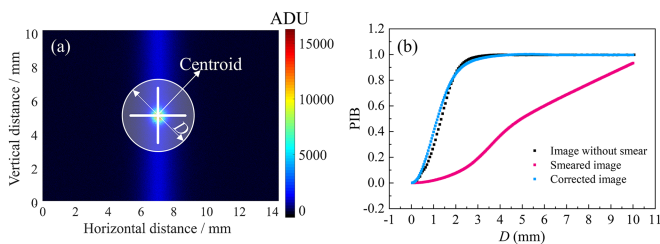

Fig. 8.   (a) Schematic diagram of PIB. (b) PIB curves of different images.

and intensity distribution of the spot, and the beam divergence angle is calculated by the binominal fitting of the beam width.

According to Fig. 7(a) and (c), M^2 without smear effect taken by the CMOS camera is 4.2158, while M^2 of the corrected spot taken by CCD camera is 4.1004, with an error of less than 3%, which generally meets the requirements of BQM. It is a typical multimode laser M^2, which is about 2∼10. For the smeared spots in Fig. 7(b), the centroid coordinates and beam width cannot be accurately obtained due to line noise, so the beam divergence angle cannot be effectively binomially fitted.

To further discuss the correction effect of single image, power in the bucket (PIB) is selected. It is the ratio of the total power within diameter D to that of the image, and the area within D is centered on the spot centroid, as shown in Fig. 8(a). PIB can be used to calculate the beam width, which is the basis of BQM. Generally, D corresponding to PIB = 86.5% is selected as the beam width. Take the images in the focal plane from the sequences in Fig. 7 as an example. Fig. 8(b) shows PIB varying with D of the images. By the curves, the beam width measurement error of the corrected image does not exceed 4%.

Without a control group, there is also a convenient and effective evaluating standard in the practical application. It can be noted that the PIB slope of the smeared image cannot remain zero in Fig. 8(b). The reason is that the significant line noise in the area outside the spot makes PIB continue increasing. It is also why the beam divergence angle cannot be effectively binomially fitted in the calculation of M^2. Given the row similarity of the line noise, whether the PIB slope is close to zero at the curve end can judge whether the correction meets the requirements of BQM.

V. Conclusion

This paper proposes a correction method of the smeared image from IT-CCD in BQM. Its mathematical model, implementation process and experimental results are investigated. The conclusions are followed.

1) The smear effect from IT-CCD in BQM performs as the superposition of the main line noise caused by light penetration and the sub-lines noise. The sub-lines are linearly related to the main line, and their total noise and optical signal also follow the relationship expression that can be deduced. The pre-calibration of the camera can obtain the expression parameters at the working wavelength. According to the above expression, the smeared image can be corrected in the next measuring.

2) The correction is used for the cross-section spots of different shapes, intensities, imaging modes and exposure times to discuss the broad application of the method.

3) A multimode laser's beam quality factor M^2 is calculated with the correction for the image sequence, and an error less than 3% verifies the correct effect. Correspondingly, PIB is selected for a single image, and an error of beam width is less than 4%.

4) PIB is proposed as the evaluation function without a control group. If the PIB slope tends to zero at the curve end, the smear correction meets the requirement of BQM.

This work proposes a new research idea for smeared images. Here are some possible further development directions based on this work.

1) Further research can be carried out on the smeared image features of IT-CCD, especially the causes of its formation are supposed to be traced from the photoelectric structure and signal processing of sensors and cameras.

2) Experiments can be conducted for lasers with different wavelengths, and the stable correction methods for broad spectrum can be discussed.

3) For the smeared image caused by light penetration in other fields, if no sub-lines are found, it is feasible to only deal with the main line based on the idea of this work, which is the correction according to the correlation between the noise and the optical signal.

Acknowledgment

References

[1] K. E. Sumachev, V. V. Sharkov, A. P. Savikin, and I. A. Grishin, "Measurement of 1.94 μm YAP:Tm^{3+} laser beam quality using a CCD camera," *J. Opt. Technol.*, vol. 87, no. 5, pp. 262–265, May 2020, doi: 10.1364/JOT.87.000262.

[2] J. A. Ruff and A. E. Siegman, "Single-pulse laser beam quality measurements using a CCD camera system," *Appl. Opt.*, vol. 31, no. 24, pp. 4907–4909, Aug. 1992, doi: 10.1364/AO.31.004907.

[3] C. S. Lim, M. H. Hong, A. Senthil Kumar, M. Rahman, and T. C. Chong, "Study of field intensity distribution of laser beam propagating through a micro-lens array," *Appl. Phys. A*, vol. 107, no. 1, pp. 149–153, Apr. 2012, doi: 10.1007/s00339-012-6776-y.

[4] V. S. Yu, C. Tatyana Yu, and V. K. Alexis, "Analysis of the laser intensity distribution," *Proc. SPIE*, vol. 4900, 2002, pp. 367–372, doi: 10.1117/12.484582.

[5] J. T. Bosiers, I. M. Peters, C. Draijer, and A. Theuwissen, "Technical challenges and recent progress in CCD imagers," *Nucl. Instrum. Methods Phys. Res. Sect. A: Accelerators, Spectrometers, Detectors Assoc. Equip.*, vol. 565, no. 1, pp. 148–156, Sep. 2006, doi: 10.1016/j.nima.2006.05.033.

[6] W. Guo, L. Jin, and J. Xiong, "Driving techniques for high frame rate CCD camera," *Proc. SPIE*, vol. 6833, 2007, Art. no. 683339, doi: 10.1117/12.760841.

[7] S. Wang et al., "A 47 million pixel high-performance interline CCD image sensor," *IEEE Trans. Electron Devices*, vol. 63, no. 1, pp. 174–181, Jan. 2016, doi: 10.1109/TED.2015.2447214.

[8] S. Wang et al., "43- and 50-Mp high-performance interline CCD image sensors," *IEEE Trans. Electron Devices*, vol. 66, no. 3, pp. 1329–1337, Mar. 2019, doi: 10.1109/TED.2019.2891414.

[9] H. Ono, T. Ozaki, H. Tanaka, and Y. Kawamoto, "Analysis of smear noise in interline-CCD image sensor with gate-free isolation structure," *Japanese J. Appl. Phys.*, vol. 30, no. 12B, pp. 3621–3626, Dec. 1991, doi: 10.1143/jjap.30.3621.

[10] A. Tanabe et al., "Dynamic range improvement by narrow-channel effect suppression and smear reduction technologies in small pixel IT-CCD image sensors," *IEEE Trans. Electron Devices*, vol. 47, no. 9, pp. 1700–1706, Sep. 2000, doi: 10.1109/16.861580.

[11] K. Ishikawa et al., "IT CCD imaging sensor with variable speed electronic shutter," *Proc. SPIE*, vol. 1107, 1989, pp. 65–76, doi: 10.1117/12.960651.

[12] T. Kumesawa, M. Yamamura, H. Terakawa, H. Murata, H. Matsumoto, and S. Ochi, "High-resolution CCD image sensors with reduced smear," *IEEE Trans. Electron Devices*, vol. ED-32, no. 8, pp. 1451–1456, Aug. 1985, doi: 10.1109/T-ED.1985.22144.

[13] E. G. Stevens et al., "Recent enhancements to interline and electron multiplying CCD image sensors," *Sensors*, vol. 17, no. 12, Dec. 2017, Art. no. 2841, doi: 10.3390/s17122841.

[14] N. Teranishi and Y. Ishihara, "Smear reduction in the interline CCD image sensor," *IEEE Trans. Electron Devices*, vol. 34, no. 5, pp. 1052–1056, May 1987, doi: 10.1109/T-ED.1987.23043.

[15] A. C. Douglas et al., "High performance 7.4-micron interline transfer CCD platform for applied imaging markets," *Proc. SPIE*, vol. 8659, 2013, Art. no. 865908, doi: 10.1117/12.982017.

[16] A. C. Douglas et al., "New 5.5 μm interline transfer CCD platform for applied imaging markets," *Proc. SPIE*, vol. 7249, 2009, Art. no. 72490C, doi: 10.1117/12.806389.

[17] K. Koji, M. Shinji, U. Yoshinori, K. Hiroe, and H. Teruo, "Simulation for estimating smear noise and sensitivity of CCD image sensors having square pixels cells less than 2.0 μm," *Proc. SPIE*, vol. 6501, 2007, Art. no. 650105, doi: 10.1117/12.704631.

[18] T. T. Bojan and J. Y. George, "Elimination of artifacts in interline charge-coupled devices imagers," *Opt. Eng.*, vol. 30, no. 10, pp. 1542–1546, Oct. 1991, doi: 10.1117/12.55959.

[19] Y. S. Han, E. Choi, and M. G. Kang, "Smear removal algorithm using the optical black region for CCD imaging sensors," *IEEE Trans. Consum. Electron.*, vol. 55, no. 4, pp. 2287–2293, Oct. 2009, doi: 10.1109/TCE.2009.5373800.

[20] Y. Zhang, L. G. Zhang, and X. X. Zhang, "Real-time elimination of smear noise for large interline transfer area CCD camera," *Opt. Precis. Eng.*, vol. 21, no. 9, pp. 2388–2394, Sep. 2013, doi: 10.3788/OPE.2013 2109.2388.

[21] W. M. Owen, H. A. Weaver, and A. Cheng, "A quick method for removing a CCD electronic shutter's two-sided smear," *Pub. Astronomical Soc. Pacific*, vol. 132, no. 1007, Dec. 2019, Art. no. 014504, doi: 10.1088/1538-3873/ab583f.

[22] K. Powell, D. Chana, D. Fish, and C. Thompson, "Restoration and frequency analysis of smeared CCD images," *Appl. Opt.*, vol. 38, no. 8, pp. 1343–1347, Mar. 1999, doi: 10.1364/AO.38.001343.

[23] F. A. Iglesias, A. Feller, and K. Nagaraju, "Smear correction of highly variable, frame-transfer CCD images with application to polarimetry," *Appl. Opt.*, vol. 54, no. 19, pp. 5970–5975, Jul. 2015, doi: 10.1364/AO.54.005970.

[24] T. Bakker, D. Turner, and J. Battaglia, "Development of a miniature ingaas camera for wide operating temperature range using a temperature-parameterized uniformity correction," *Proc. SPIE*, vol. 6940, 2008, Art. no. 69400K, doi: 10.1117/12.780007.